Nanoscale Advances

ROYAL SOCIETY OF CHEMISTRY

PAPER

View Article Online
View Journal | View Issue

Cite this: *Nanoscale Adv.*, 2023, **5**, 6695

Exploring dual solutions and thermal conductivity in hybrid nanofluids: a comparative study of Xue and Hamilton–Crosser models

Mahnoor Sarfraz, Muhammad Yasir * and Masood Khan

Hybrid nanofluids show great potential for heat transport applications such as solar thermal systems, car cooling systems, heat sinks, and thermal energy storage. They possess better thermal stability and properties compared to standard nanofluids. In this study, a base fluid, methanol, is injected into an electrically conducting heat-generating/absorbing disk of permeable boundary, and dual solutions are obtained. Two alternative models, Xue and Hamilton–Crosser are considered, and their thermal conductivities are contrasted. Furthermore, thermal radiation and ohmic heating are also considered, and convective boundary conditions are utilized to simulate overall heat gains or losses resulting from conduction, forced or natural convection between nearby objects of nearly constant temperature. Using a similarity transform, the governing equations are obtained and numerically solved *via* bvp4c, a finite difference method. It is observed that the presence of a magnetic field and the shrinking of the disk elevate the energy transport rate and wall stress. Additionally, the skin friction coefficient and thermal distribution rate increase with wall transmission constraint while fluid flow and energy transport diminish. Furthermore, particle clustering and nano-layer creation suggest that the Hamilton–Crosser model exhibits better thermal conductivity than the Xue model.

Received 9th July 2023
Accepted 4th November 2023

DOI: 10.1039/d3na00503h

rsc.li/nanoscale-advances

1. Introduction

Studies on nanofluid flow frequently prioritize the flow's thermal conductivity and heat transmission characteristics, while its thermophysical properties are often overlooked. However, including multiple nanoparticles in a base fluid can significantly increase the heat transfer phenomena. Hybrid nanofluids, composed of metal, polymeric, or non-metallic composite nanoparticles or a combination of different nanoparticles distributed in a base fluid, outperform traditional nanofluids with better pressure drop and heat transfer properties. The efficacy of ternary nanofluids is strongly influenced by the types, shapes, sizes, and percentages of the nanoparticles utilized. The revolutionary concept of carbon nanotubes was first introduced by Iijima[1] through experimentation, resulting in the discovery of microscopic carbon layer straws known as carbon nanotubes. Although the essential components of the liquid were still complex hydrocarbon molecules, Choi and Eastman[2] used the term "nanofluid" to describe fixed nanoscale particles floating in a fluid medium (nano-lubricants). Hybrid nanofluids possess exceptional mechanical, electrical, and thermal properties, as well as high electrical and thermal conductivities, making them strong and lightweight. Several studies on the applications of hybrid nanofluids are addressed in ref. 3–11. Moldoveanu *et al.*[12] scrutinized the thermal conductivity of two nanofluids and their hybrid, and the experimental outcomes were presented at various temperatures and volume fractions, including room temperature.

Convective heat transfer models can present non-linearity issues and dual solutions, which can result in complex behaviors. Therefore, it is essential to understand both stable and unstable states. To address this, several studies have been conducted on different scenarios. For instance, Zheng *et al.*[13] explored the radiation effect on velocity and temperature fields in a quiescent micropolar fluid with nonlinear power-law surface velocity and temperature distributions. In a similar study, Mahapatra *et al.*[14] investigated dual solutions in magnetohydrodynamic stagnation-point flow and heat transfer over a shrinking surface with partial slip, while Rostami *et al.*[15] developed an analytical solution for the steady laminar MHD mixed convection boundary layer flow of a SiO_2–Al_2O_3/water hybrid nanofluid near the stagnation point on a vertical flat plate. Moreover, Mousavi *et al.*[16] studied the dual solutions for Casson hybrid nanofluid flow due to a stretching/shrinking sheet with suction, radiation, and convective boundary condition effects. Asjad *et al.*[17] introduced a new fractional operator to model memory effects and solved analytically for temperature and velocity fields using the Laplace transform approach. Studies of heat transport are discussed in further studies, as reported in ref. 18–28.

Department of Mathematics, Quaid-i-Azam University, Islamabad 44000, Pakistan. E-mail: myasir@math.qau.edu.pk

Drawing inspiration from the aforementioned studies, it is formulated that the premise that the base fluid, methanol (CH_3OH), is comprised of a blend of silica (SiO_2) and alumina (Al_2O_3), forming a disk with a porous boundary capable of generating and absorbing heat. The problem's coordinates take the form of a cylinder (r,θ,z), with the thermal conductivities of the two alternative models: Xue and Hamilton–Crosser, compared. The surface is seen to radially expand and contract with time, with convective boundary conditions provided. A uniform magnetic field is applied perpendicularly to the z-axis, with minimal interference from the electric field. Furthermore, both thermal radiation and ohmic heating effects are taken into consideration. The dimensionless equations are obtained through similarity profiles and numerically solved using bvp4c. The novelty of this study is in using these nanomaterials and the effects taken. Methanol-based hybrid nanofluids incorporating silica and alumina nanoparticles have demonstrated a significant increase in heat transport efficiency, attributed to their high thermal conductivities and extensive surface area. These hybrid nanomaterials have garnered attention for superior rheological, thermal, and economic performance compared to monotype nanofluids. They enhance convective heat transfer, reduce boundary layer thickness, and provide thermal stability, making them indispensable for diverse applications such as solar thermal systems, car cooling, and heat sinks.

The article is structured into four distinct sections. In Section 2, the mathematical problem at hand is comprehensively addressed, providing a detailed insight into the complex computations and analytical techniques employed to obtain the desired results. Section 3 is devoted to graphical illustrations, accompanied by their corresponding physical significance, which helps readers visualize the intricate details of the problem and facilitates better understanding. Finally, Section 4 presents a concise summary of the findings, highlighting the key takeaways from the study and providing insights for future research in this area.

2. Problem formulation

In this study, hybrid nanofluids consisting of silica and alumina nanoparticles in methanol are considered, which have been shown to exhibit excellent cooling properties. The disk's boundary is assumed to be porous, allowing heat generation and absorption. The problem is analyzed using cylindrical coordinates (r,θ,z), and the velocity field $\mathbf{V}$ is characterized by the components $[\tilde{u}(r,t), \tilde{w}(r,t)]$. The thermal conductivity of two models is considered, namely Xue and Hamilton–Crosser. The surface of the disk is assumed to be radially expanding or contracting, which leads to a velocity component along the boundary of $\tilde{u}_w = \frac{Cr}{1-\alpha t}$. In the far-field region near the stagnation point, the velocity is given by $\tilde{u}_\infty = \frac{ar}{1-\alpha t}$. A uniform magnetic field $\mathbf{B} = [0, 0, B_0]$ is applied perpendicular to the z-axis, and the effects of the electric field are assumed to be negligible. The study also considers the effects of ohmic heating and thermal radiation. The surface of the disk is heated by convection from a hot fluid with temperature $\tilde{T}_w$ and heat transfer coefficient h_w, while the ambient temperature distribution is represented by $\tilde{T}_\infty$.

To assist in understanding, Fig. 1 displays the geometry of the problem, while Table 1 presents the thermophysical characteristics of both the methanol and alumina–silica nanoparticles.

The governing equations are (see ref. 16)

$$\frac{\partial(\tilde{u}r)}{\partial r} + \frac{\partial(\tilde{w}r)}{\partial z} = 0, \tag{1}$$

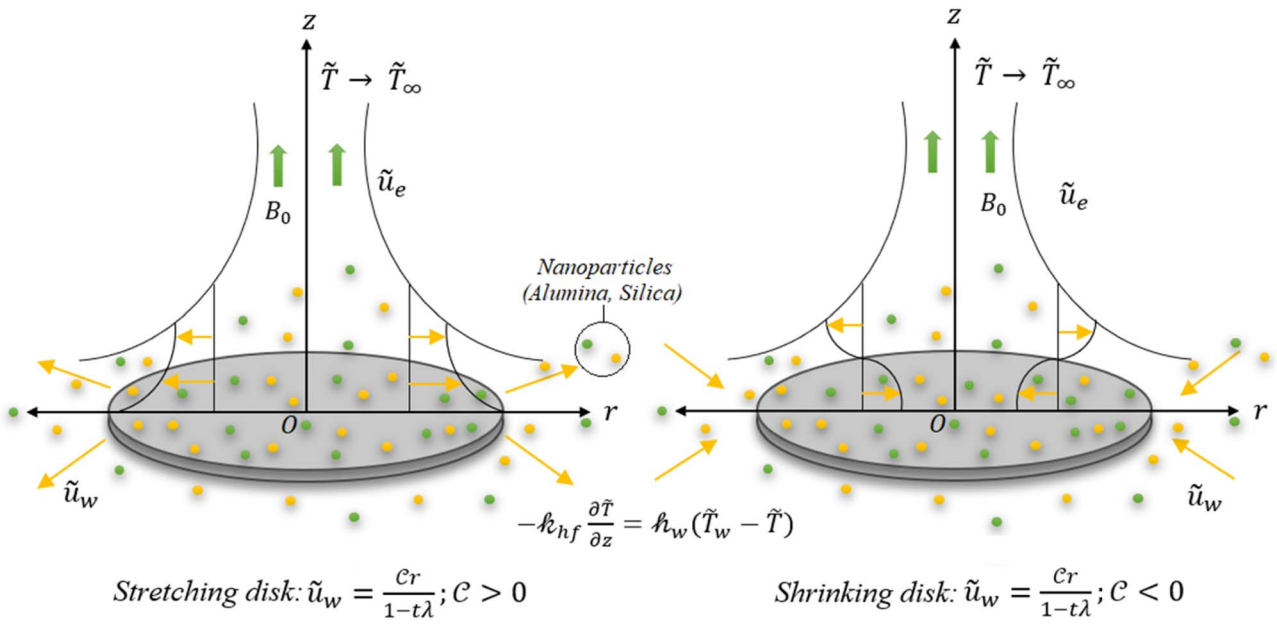

Fig. 1 Flow mechanism.

Table 1 Numerical values for the thermophysical features

	Base fluid	Nanoparticles	
Physical properties	CH_3OH	SiO_2	Al_2O_3
ϱ_f	792	2650	3970
c_p	2545	730	765
k	0.2035	1.5	40
Pr at 25 °C	6.83	—	—
s	3.7 (spherical)		

$$\frac{\partial \tilde{u}}{\partial t}+\tilde{u}\frac{\partial \tilde{u}}{\partial r}+\tilde{w}\frac{\partial \tilde{u}}{\partial z}=\frac{\partial \tilde{u}_\infty}{\partial t}+\frac{\tilde{u}_\infty \partial \tilde{u}_\infty}{\partial r}+\frac{\mu_{hn}}{\varrho_{hn}}\left(\frac{\partial^2 \tilde{u}}{\partial z^2}\right)-\frac{\sigma {B_0}^2}{\varrho_{hn}}(\tilde{u}-\tilde{u}_\infty), \tag{2}$$

$$\frac{\partial \tilde{T}}{\partial t}+\tilde{u}\frac{\partial \tilde{T}}{\partial r}+\tilde{w}\frac{\partial \tilde{T}}{\partial z}=\frac{k_{hn}}{(\varrho c_p)_{hn}}\left(\frac{\partial^2 \tilde{T}}{\partial z^2}\right)-\frac{1}{(\varrho c_p)_{hn}}\frac{\partial q_{rad}}{\partial z}+\frac{Q^*}{(\varrho c_p)_{hn}}\left(\tilde{T}-\tilde{T}_\infty\right)+\frac{\mu_{hn}}{(\varrho c_p)_{hn}}\left(\frac{\partial \tilde{u}}{\partial z}\right)^2, \tag{3}$$

where $q_{rad}=-\frac{16\sigma^*{\tilde{T}_\infty}^3}{3k^*}\frac{\partial \tilde{T}}{\partial z}$ is radiative heat flux.

The thermophysical properties are given as (see ref. 7)

$$\left.\begin{aligned}\mu_{hn}&=\mu_f\left(1-\phi_{Al_2O_3}\right)^{-2.5}\left(1-\phi_{SiO_2}\right)^{-2.5},\\ \varrho_{hn}&=\phi_{SiO_2}\varrho_{SiO_2}+\left(1-\phi_{SiO_2}\right)\left[\left(1-\phi_{Al_2O_3}\right)\varrho_f+\phi_{Al_2O_3}\varrho_{Al_2O_3}\right],\\ (\varrho c_p)_{hn}&=\phi_{SiO_2}(\varrho c_p)_{SiO_2}+\left(1-\phi_{SiO_2}\right)\left[\left(1-\phi_{Al_2O_3}\right)(\varrho c_p)_f+\phi_{Al_2O_3}(\varrho c_p)_{Al_2O_3}\right],\end{aligned}\right\} \tag{4}$$

For Hamilton–Crosser model, the thermal conductivity is given as

$$\frac{k_{hn}}{k_n}=\frac{k_{SiO_2}+(s-1)k_n-(s-1)\phi_{SiO_2}(k_n-k_{SiO_2})}{k_{SiO_2}+(s-1)k_n+\phi_{SiO_2}(k_n-k_{SiO_2})},\ \frac{k_n}{k_f}=\frac{k_{Al_2O_3}+(s-1)k_f-(s-1)\phi_{Al_2O_3}(k_f-k_{Al_2O_3})}{k_{Al_2O_3}+(s-1)k_f+\phi_{Al_2O_3}(k_f-k_{Al_2O_3})}. \tag{5}$$

The value of s vary for different shapes, such as for spherical $s=3.0$. For Xue model, the thermal conductivity is given as

$$\frac{k_{hn}}{k_n}=\frac{\left(1-\phi_{SiO_2}\right)+2\phi_{SiO_2}\left(\frac{k_{SiO_2}}{k_{SiO_2}-k_n}\right)\ln\left(\frac{k_{SiO_2}+k_n}{2k_n}\right)}{\left(1-\phi_{SiO_2}\right)+2\phi_{SiO_2}\left(\frac{k_{bf}}{k_{SiO_2}-k_n}\right)\ln\left(\frac{k_{SiO_2}+k_n}{2k_n}\right)},\ \frac{k_n}{k_f}=\frac{\left(1-\phi_{Al_2O_3}\right)+2\phi_{Al_2O_3}\left(\frac{k_{Al_2O_3}}{k_{Al_2O_3}-k_f}\right)\ln\left(\frac{k_{Al_2O_3}+k_f}{2k_f}\right)}{\left(1-\phi_{Al_2O_3}\right)+2\phi_{Al_2O_3}\left(\frac{k_f}{k_{Al_2O_3}-k_f}\right)\ln\left(\frac{k_{Al_2O_3}+k_f}{2k_f}\right)}, \tag{6}$$

The boundary conditions (BCs) are (see ref. 16)

$$\tilde{u}=\tilde{u}_w=\frac{Cr}{1-\alpha t},\ \tilde{w}=w_0,\ -k_{hn}\frac{\partial \tilde{T}}{\partial z}=h_w\left(\tilde{T}_w-\tilde{T}\right)\ \text{at}\ z=0, \tag{7}$$

$$\tilde{u}=\tilde{u}_\infty\to\frac{ar}{1-\alpha t},\ \tilde{T}\to\tilde{T}_\infty,\ \text{as}\ z\to\infty. \tag{8}$$

Introducing stream function $\psi=\frac{-r^2\tilde{u}_\infty}{\sqrt{\mathrm{Re}_r}}\tilde{f}(\zeta)$, where $\zeta=\frac{z}{r}\sqrt{\mathrm{Re}_r}$ and local Reynolds number $\mathrm{Re}_r=\frac{r\tilde{u}_\infty}{\nu_f}$ with the following similarity ansatz

$$\left.\begin{aligned}\tilde{u}=-\frac{1}{r}\frac{\partial \psi}{\partial z}=\frac{ar\tilde{f}'(\zeta)}{1-\alpha t},\ \tilde{w}=\frac{1}{r}\frac{\partial \psi}{\partial r}=-2\left(\frac{a\nu_f}{1-\alpha t}\right)^{\frac{1}{2}}\tilde{f}(\zeta),\\ \tilde{T}=\tilde{T}_\infty+\left(\tilde{T}_w-\tilde{T}_\infty\right)\tilde{\theta}(\zeta),\ t<\frac{1}{\alpha}.\end{aligned}\right\} \tag{9}$$

The negative sign in eqn (9) indicates that the fluid at the far-field is being pulled towards the surface, rather than being pushed away from it. Using eqn (11)

$$\tilde{f}'''+\mathcal{A}_1\mathcal{A}_2\left[2\tilde{f}\tilde{f}''+1-\left(\tilde{f}'\right)^2+\lambda\left(1-\tilde{f}'-\frac{\zeta\tilde{f}''}{2}\right)\right]-M^2\mathcal{A}_1\left(\tilde{f}'-1\right)=0, \tag{10}$$

$$\left(1+\frac{4R_d}{3\mathcal{A}_4}\right)\tilde{\theta}''+\mathrm{Pr}\frac{\mathcal{A}_3}{\mathcal{A}_4}\left(\tilde{f}\tilde{\theta}'-\frac{\zeta\lambda\tilde{\theta}'}{2}\right)+\frac{\mathcal{A}_1}{\mathcal{A}_4}\mathrm{Br}\left(\tilde{f}''\right)^2+\frac{\mathrm{Pr}Q^*}{\mathcal{A}_4}\tilde{\theta}=0, \tag{11}$$

$$\tilde{f}(0)=\tilde{f}_w,\tilde{f}'(0)=\chi,\tilde{f}'(\infty)=1,\tilde{\theta}'(0)=\frac{\beta_i}{\mathcal{A}_4}\left[\tilde{\theta}(0)-1\right],\tilde{\theta}(\infty)=0, \tag{12}$$

where for ternary hybrid nanofluids

$$\mathcal{A}_1=\frac{\mu_{hn}}{\mu_n},\ \mathcal{A}_2=\frac{\varrho_{hn}}{\varrho_n},\ \mathcal{A}_3=\frac{(\varrho c_p)_{hn}}{\varrho_n},\ \mathcal{A}_4=\frac{k_{hn}}{k_n}, \tag{13}$$

The dimensionless parameters are

$$M=\sqrt{\frac{\sigma_f {B_0}^2}{a\varrho_f}},\ \tilde{f}_w=\frac{-w_0}{\sqrt{a\nu_f}},\ \mathrm{Br}=\mathrm{PrEc},\ \mathrm{Pr}=\frac{(\varrho c_p)_f}{k_f},\ \mathrm{Ec}=\frac{{\tilde{u}_\infty}^2}{\left(\tilde{T}_w-\tilde{T}_\infty\right)c_p},$$
$$\chi=\frac{C}{a},\ \delta=\frac{\alpha}{a},\ Q^*=\frac{Q_0}{a(\varrho c_p)_f},\ \beta_i=\frac{h_w}{k_f}\sqrt{\frac{a}{\nu_f}},\ R_d=\frac{4\sigma^*{\tilde{T}_\infty}^3}{k^*k_f}. \tag{14}$$

The quantities of engineering interest, $\tilde{C}_f$ and Nu_r are given as

$$\tilde{C}_f=\frac{\tau_{rz}}{\varrho_f{\tilde{u}_w}^2},\quad \text{where } \tau_{rz}=\mu_{hn}\left[\frac{\partial\tilde{u}}{\partial z}\right]_{z=0},$$
$$\tilde{C}_f=\frac{2\mu_{hn}}{\sqrt{\mathrm{Re}_r}\mu_n}\tilde{f}''(0), \tag{15}$$

$$\mathrm{Nu}_r=\frac{-k_{hn}r}{k_f\left(\tilde{T}_w-\tilde{T}_\infty\right)}\left[\frac{\partial\tilde{T}}{\partial z}\right]_{z=0}+\left[q_{rad}\right]_{z=0},$$
$$\mathrm{Nu}_r=-\left(\frac{k_{hn}}{k_n}+\frac{4R_d}{3}\right)\tilde{\theta}'(0). \tag{16}$$

3. Interpretation and analysis of results

This section presents an analysis of the numerical results obtained for various relevant parameters, such as velocity and temperature distributions, and the effects of control parameters on Nu_r and $\tilde{C}_f$. This study presents the solution of boundary value problems (BVPs) for ordinary differential equations using MATLAB's bvp4c function. Our approach is based on using a finite difference method to discretize the BVP, which allows us to solve the resulting system of equations using a collocation method. To achieve the desired level of accuracy, the number of mesh points is adjusted, and the initial guess is provided to the solver. The estimated error count is constantly monitored during the computation, ensuring the quality of the solution. During the calculations, some parameters are held constant, and the behavior of the first (stable) and second (unstable) solutions is examined. The considered values and ranges of the parameters are $\mathrm{Re}=0.6$, $1\le\mathrm{Pr}\le10$, $1\le\beta_i\le3$, $0.01\le\delta^*\le0.05$, $0.5\le\tilde{f}_w\le4$, $0.01\le\mathrm{Ec}\le0.08$, $0.01\le M\le2$, and $0.1\le\lambda\le2$, and spherical shaped nanoparticles are used. The behavior of a mixture of nanoparticles, namely silica and alumina, submerged into a solution of methanol, *i.e.*, (SiO_2–Al_2O_3/CH_3OH), is examined for two different models, Xue and Hamilton–Crosser models. Solid lines represent the behavior of the first solution, while dot-dashed lines depict the second solution.

Fig. 2(a) and (b) elucidate the impact of the magnetic field parameter M on the key parameters, namely $\tilde{C}_f$ and Nu_r. Both figures represent the first and second solutions for control parameters χ and $M=0.5$, 1.0, 1.5. Fig. 2(a) demonstrates that both solutions' values of $\tilde{C}_f$ escalate with an increase in M. The critical values, $\chi_c=-3.73484$, -3.84431, -3.95486, are observed at $M=0.5$, 1.0, 1.5, respectively. This enhancement in the behavior of $\tilde{C}_f$ can be attributed to the linear increment in $\tilde{C}_f$ with the magnetic field's increase. The magnetic field induces Lorentz forces that alter the velocity profile of the fluid, resulting in changes to the skin friction coefficient. Specifically, the skin friction coefficient decreases with an increasing magnetic field due to the development of a boundary layer with lower momentum. The Lorentz force causes the flow field to decline, magnifying the frictional forces, thus augmenting $\tilde{C}_f$. On the

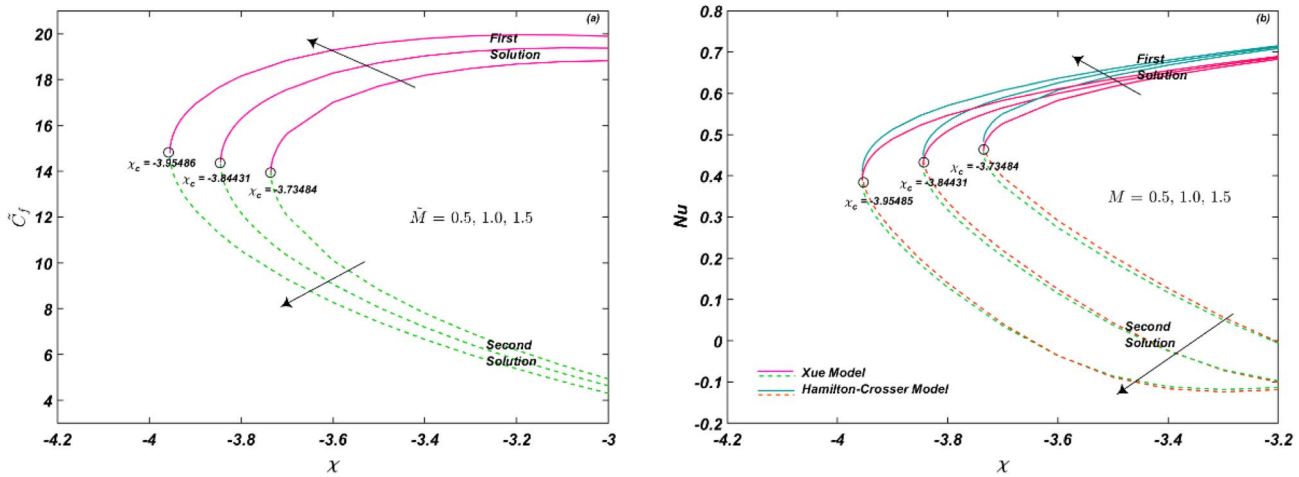

Fig. 2 (a and b) Influence of M on $\tilde{C}_f$ and Nu_r.

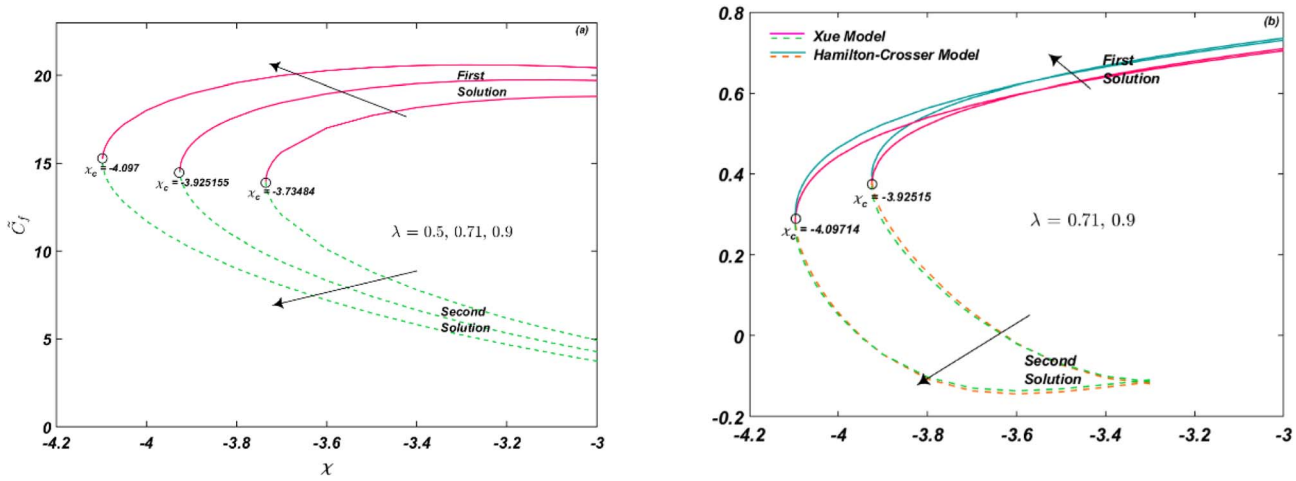

Fig. 3 (a and b) Influence of λ on $\tilde{C}_f$ and Nu_r.

other hand, Fig. 2(b) demonstrates the impact of M on Nu_r, which indicates that heat energy gains result from an increase in magnetic force, leading to chaotic particle motion. The system temperature increases due to the fluid molecules' physical energy and their greater intermolecular vibrations caused by increased kinetic energy. The magnetic field enhances fluid mixing and promote heat transfer, leading to an increase in the Nusselt number. It is noteworthy that the behavior of Xue and Hamilton–Crosser models is depicted here. The results indicate that the magnetic parameter has improved the outcomes of Nu_r. Moreover, the values for the Hamilton–Crosser models are more pronounced than the Xue model, indicating that they have better thermal conductivity than the Xue model. The critical values, $\chi_c = -3.73484, -3.84431, -3.95486$, are observed at $M = 0.5, 1.0, 1.5$, respectively.

Fig. 3(a) and (b) demonstrate the influence of unsteadiness parameter λ on $\tilde{C}_f$ and Nu_r, respectively. Critical values $\chi_c = -4.097, -3.925155, -3.73484$ at $\lambda = 0.5, 0.71, 0.9$, respectively, are observed. As depicted in Fig. 3(a), an increase in λ leads to an enhancement in $\tilde{C}_f$ (for both solutions), resulting in a linear increment over time. Physically, unsteadiness can cause a delay in fluid flow, leading to an increase in frictional forces. Conversely, Fig. 3(b) illustrates the impact λ on Nu_r, with critical values of $\chi_c = -4.097, -3.925155$ at $\lambda = 0.5, 0.71$, respectively. Augmentation in thermal transport rate occurs as a result of an increase in unsteadiness, which leads to chaotic particle motion, greater intermolecular vibrations, and increased kinetic energy, resulting in elevated system temperatures. The behavior of Xue and Hamilton–Crosser models is depicted for first and second solutions, with Hamilton–Crosser models exhibiting better thermal conductivity than the Xue model.

Fig. 4(a) and (b) depict the influence of Eckert number and Biot number on Nu_r. It can be observed that Nu_r increases with an increase in Ec, which represents the self-heating of the fluid due to dissipation effects and temperature gradients. Notably, the critical value remains the same for different values of Ec, *i.e.*, $\chi_c = -3.73484$ for $Ec = 0.01, 0.05$. On the other hand, the Biot number β_i relates the rate of heat transfer inside a solid to the rate of heat transfer at the solid's surface. It is defined as the ratio of the internal thermal resistance to the external thermal

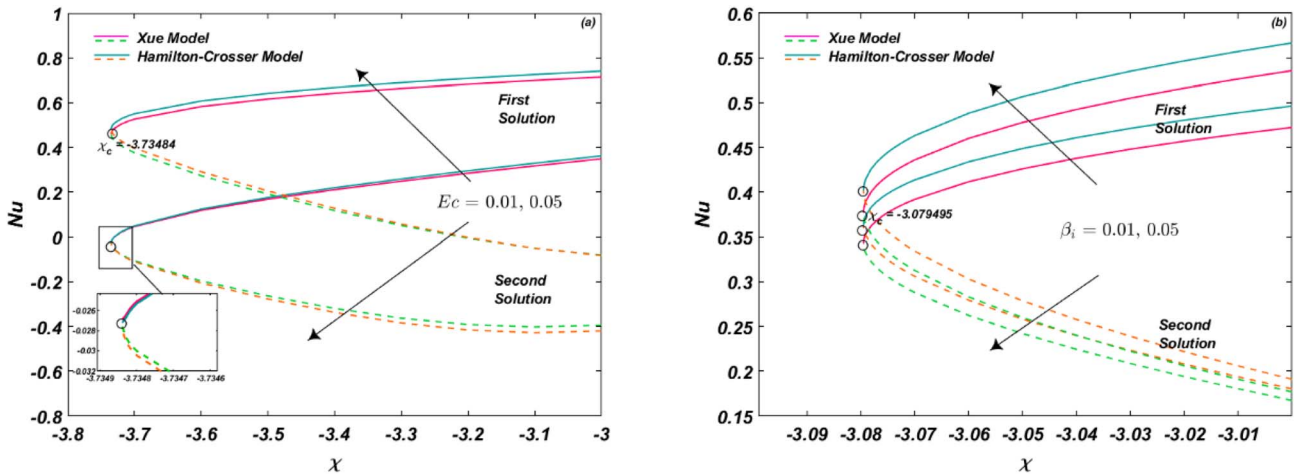

Fig. 4 (a and b) Influence of Ec and β_i on Nu_r.

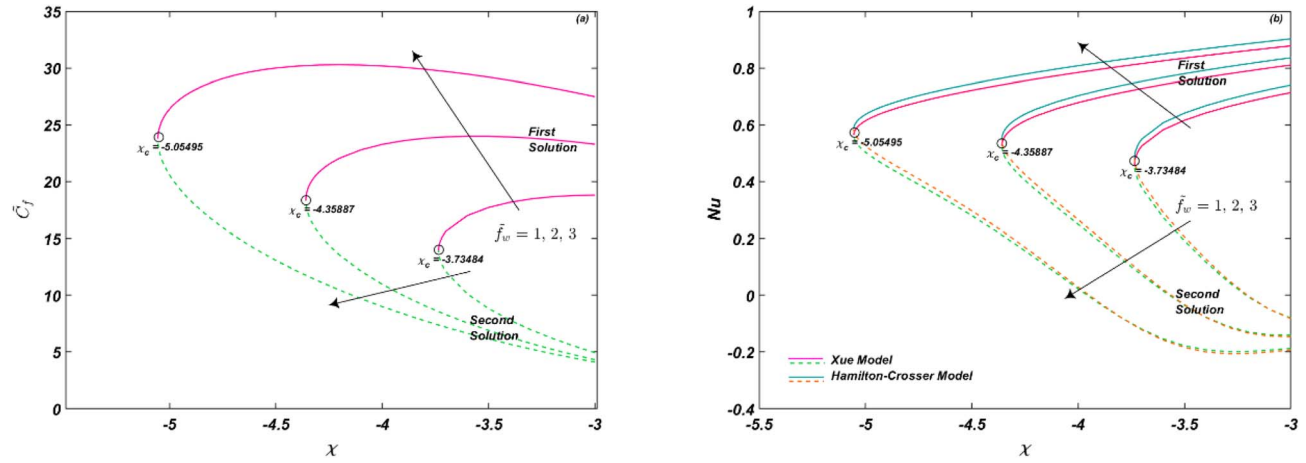

Fig. 5 (a and b) Influence of $\tilde{f}_w$ on $\tilde{C}_f$ and Nu_r.

resistance. Fig. 4(b) demonstrates that an increase in β_i leads to an increase in thermal transport rate. The critical value is $\chi_c = -3.079495$ for $\beta_i = 0.01, 0.05$. In general, the Nu_r increases with increasing Biot number. This is because as the β_i increases, the thermal resistance of the solid becomes smaller compared to the thermal resistance of the fluid, and the temperature gradient in the fluid becomes more uniform. This leads to increased heat transfer from the solid to the fluid, and therefore a higher convective heat transfer coefficient, resulting in a higher Nu_r.

The impression of $\tilde{f}_w$ is noted in Fig. 5(a) and (b) on $\tilde{C}_f$ and Nu_r, respectively. The mass transmission constraint shows the effect of suction ($\tilde{f}_w > 0$) and injection ($\tilde{f}_w < 0$). When $\tilde{f}_w > 0$, fluid suction at the surface lowers the viscous effects closer to the wall. Suction has the potential to lower fluid velocity $\tilde{f}'(\zeta)$, whereas blowing or injection has the opposite effects. As a result, greater suction velocities yield higher entertainment velocities. Thus, suction causes the fluid's velocity to decrease, while blowing causes it to increase, as shown in Fig. 6(a). Therefore, $\tilde{C}_f$ improves for $\tilde{f}_w > 0$, as shown in Fig. 5(a). On the other hand, energy of the system is declined as given in Fig. 6(b). However, Fig. 5(b) depicts that Nu_r is an increasing function of $\tilde{f}_w$ as well. It is seen that the thermal conductivity of Hamilton–Crosser's model is more than as compared to Xue's model. The critical values for Fig. 5(a) and (b) are $\chi_c = -3.73484$, -4.35887, -5.05495 at $\tilde{f}_w = 1, 2, 3$, respectively.

The behavior of shrinking/stretching parameter χ is noted in Fig. 7(a) and (b) on flow and energy distribution. The parameter shows the effect of stretching ($\chi > 0$) and shrinking ($\chi < 0$). It is illustrated that shrinking causes the flow field to decline for both solutions, as shown in Fig. 7(a). However, the temperature profile is boosted significantly for both models, as given in Fig. 7(b). Whereas it is seen that due to particle clustering and nano-layer creation, the thermal conductivity of Hamilton–Crosser is better than Xue model.

Fig. 8(a) and (b) provide an insight into the impact of Prandtl number Pr and heat generation/absorption parameter δ^* on the system's behavior. The Prandtl number is a ratio of momentum to thermal diffusivity, indicating the dominance of thermal diffusion mechanism for a given fluid. The value of Pr for methanol at 25 °C is 6.83, much higher than that of air (Pr = 0.71). A lower value of Pr signifies the prevalence of heat

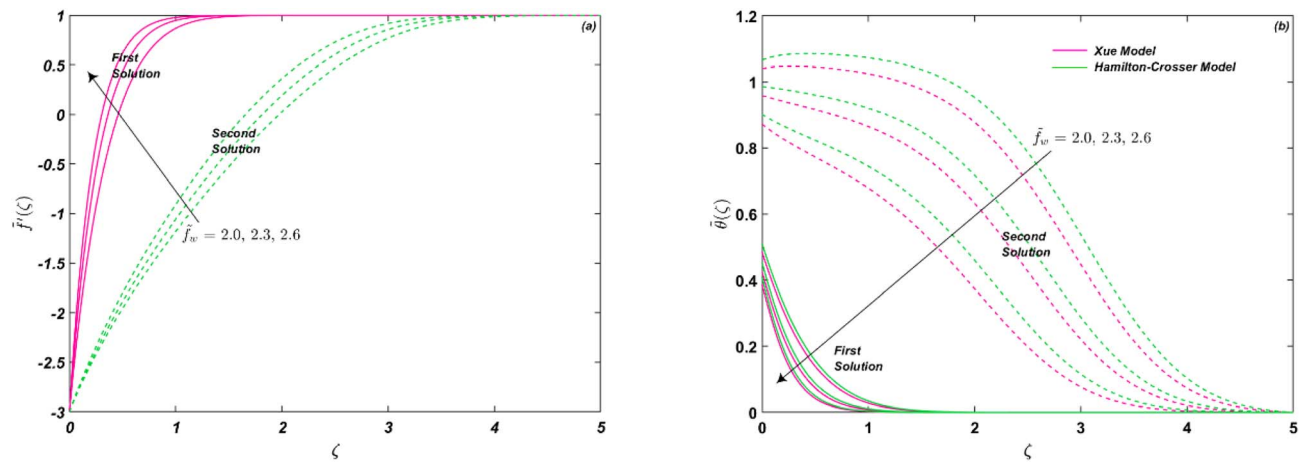

Fig. 6 (a and b) Influence of $\tilde{f}_w$ on $\tilde{f}'(\zeta)$ and $\tilde{\theta}(\zeta)$.

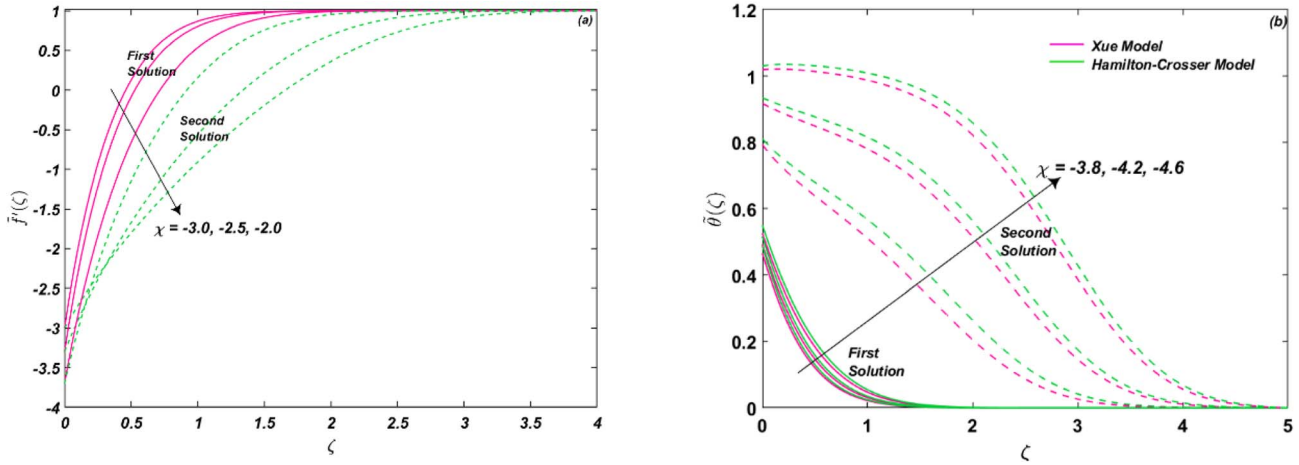

Fig. 7 (a and b) Influence of χ on $\tilde{f}'(\zeta)$ and $\tilde{\theta}(\zeta)$.

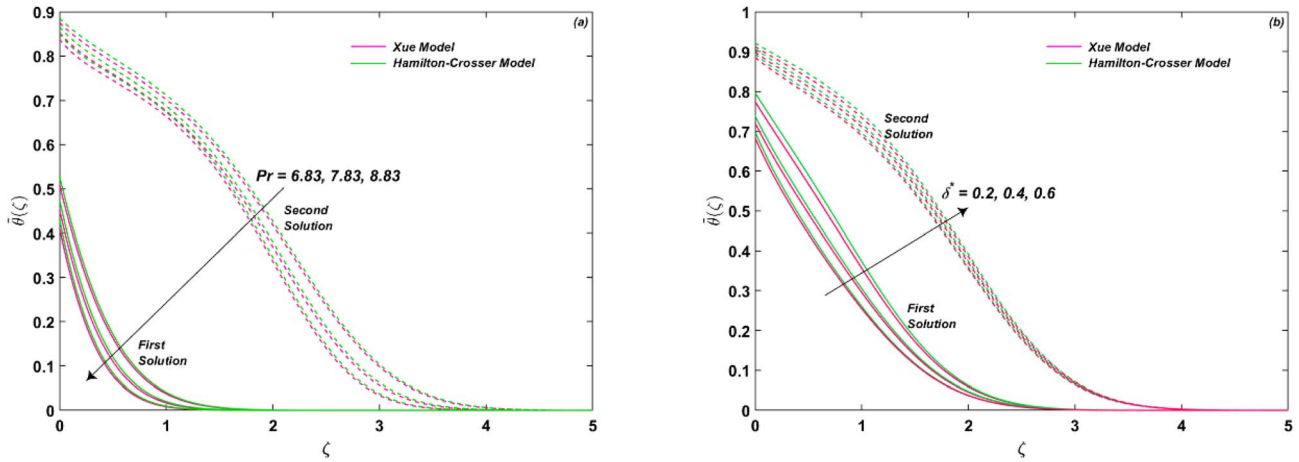

Fig. 8 (a and b) Influence of Pr and δ^* on $\tilde{\theta}(\zeta)$.

conduction over convection, where heat diffuses faster than fluid velocity. In general, Pr for gases ranges around 0.7, while it varies between 1 and 10 for fluids. Fig. 8(a) indicates that the thermal transport decreases with increasing Pr, implying that a higher Pr value leads to a significant reduction in temperature/energy transport. The presence of a heat source or sink has a significant effect on the temperature distribution in a system. A heat source increases the temperature in its vicinity, while a heat sink reduces it. This effect propagates through the system *via* heat transfer mechanisms such as conduction, convection, and radiation. The magnitude of the effect depends on the strength and location of the heat source or sink, as well as the thermal properties and boundary conditions of the system. The effect of a heat source or sink can be used to control or optimize temperature distribution in a system $\tilde{\theta}(\zeta)$, as shown in Fig. 8(b).

By contrasting the existing numerical values $\tilde{C}_f$ with the prior results, the current model in Table 2 is validated. The variation of $\chi < 0$ is presented in the absence of nanoparticles and magnetic field. It is seen that the coefficient of skin friction enhanced significantly due from $\chi = -0.25$ to -0.95.

Table 2 Comparison of $\tilde{C}_f$ for various values of χ in the absence of nanoparticles and magnetic field

			Present study
χ	Khan *et al.*[30]	Wang[29]	First solution
−0.25	1.4566365	1.456640	1.456640
−0.5	1.4900104	1.490010	1.490041
−0.75	1.3528399	1.352840	1.352838
−0.95	0.9469034	0.946900	0.946904

3.1 Stability analysis

The current research used a stability analysis to validate the obtained solution. This is of utmost significance, mainly when the governing system permits multiple-branch solutions. Identifying all probable solutions emerging from the governing boundary layer problems is essential for determining the solution. Based on previous literature studies,[31–35] the smallest eigenvalues α were plotted against χ, and the resulting Fig. 9

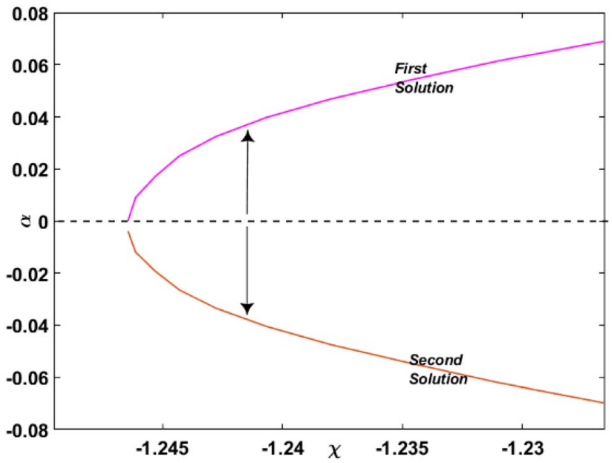

Fig. 9 Smallest eigenvalues α for χ.

was obtained. The physical interpretation of this figure is that a positive value of α indicates an initial deterioration of disturbance, implying that the flow is in a stable mode. Conversely, a negative value of α, as $\tau \to \infty$, implies that the flow is in an unstable state due to the early increase of disturbance. It should be noted that as χ approaches the critical value, $\chi_c = -1.2431$, both the stable and unstable branches converge to $\alpha = 0$. This behavior indicates that the solutions bifurcate at the critical values, and it has critical implications for the study of boundary layer problems.

4. Conclusion

An electrically conducting heat-generating/absorbing disk was assumed with a porous boundary immersed in a mixture of silica (SiO_2) and alumina (Al_2O_3) into methanol (CH_3OH) which acts as a base fluid. The thermal conductivity of two models, Xue and Hamilton–Crosser were considered and compared. The effects of MHD, heat source/sink, suction/injection, thermal radiation, and convective boundary conditions were scrutinized over a radially shrinking/stretching surface. The primary outcomes are given below.

❖ Due to particle clustering and nano-layer creation, the thermal conductivity of the Hamilton–Crosser was better than the Xue model.

❖ Energy transport rate and wall stress were elevated due to shrinking and the presence of the magnetic field.

❖ Unsteadiness declined the fluid motion, which caused the frictional forces to incline.

❖ Due to the increment in Biot number, the surface heat resistance declined, which dominated the convection mechanism resulting in a higher thermal transport rate.

❖ The critical value was the same for variation of Eckert and Biot numbers, *i.e.*, $\chi_c = -3.73484$ and -3.079495, respectively.

❖ Coefficient of skin friction and thermal distribution rate was an increasing function of wall transmission constraint, whereas the fluid flow and energy transport diminished.

❖ Incrementing Prandtl number reduced the temperature and energy transport significantly.

❖ The thermal transport was dominant due to the heat generation/absorption parameter.

Nomenclature

$(\tilde{u},\tilde{v},\tilde{w})$	Velocity components (m s^{-1})
k	Thermal conductivity (W m^{-1} K^{-1})
ν	Kinematic viscosity (m^2 s^{-1})
ϱ	Density (kg m^{-3})
$\tilde{p}$	Pressure (N m^{-2})
α	Unsteadiness rate (s^{-1})
μ	Absolute viscosity (kg m^{-1} s^{-1})
σ	Electric conductivity (Ω m)
B_0	Magnetic field strength (N s C^{-1} m^{-1})
Re_r	Reynolds number
σ^*	Stefan–Boltzmann coefficient
h_w	Heat transfer coefficient
τ_w	Wall-shear stress
$\tilde{T}$	Temperature (K)
$\tilde{f}',\tilde{\theta}$	Dimensionless velocity and temperature
$\tilde{f}_w$	Wall mass transfer coefficient
λ	Unsteadiness parameter
$\tilde{p}$	Dimensionless pressure
M	Magnetic field parameter
γ_1	Biot number
R_d	Radiation parameter
ϕ	Nanoparticle volume fraction
ζ	Dimensionless variable
k^*	Mean absorption coefficient
Pr	Prandtl number
Nu_r	Nusselt number

Subscripts

r,z	Derivative w.r.t r and z
∞	Far-field condition
w	Wall boundary condition
f	Base fluid
n	Nanofluid
hn	Hybrid nanofluid

Superscripts

$'$	Derivative w.r.t ζ

Conflicts of interest

There are no conflicts to declare.

References

1 S. Iijima, Helical microtubules of graphitic carbon, *Nature*, 1991, **354**(6348), 56–58.

2 S. U. Choi and J. A. Eastman, Enhancing thermal conductivity of fluids with nanoparticles, *Developments and Applications of Non-Newtonian Flows*, FED-vol. 231/MD-vol. 66, 1995, pp. 99–105.
3 H. Alkasasbeh, M. Swalmeh, H. Bani Saeed, F. Al Faqih and A. Talafha, Investigation on CNTs-water and human blood based Casson nanofluid flow over a stretching sheet under impact of magnetic field, *Front. Heat Mass Transfer*, 2020, **14**, DOI: 10.5098/hmt.14.15.
4 M. Sheikholeslami, E. Abohamzeh, Z. Ebrahimpour and Z. Said, Brief overview of the applications of hybrid nanofluids, *Hybrid Nanofluids*, 2022, pp. 171–202.
5 A. Kazemian, A. Salari, T. Ma and H. Lu, Application of hybrid nanofluids in a novel combined photovoltaic/thermal and solar collector system, *Sol. Energy*, 2022, **239**, 102–116.
6 G. F. Smaisim, A. M. Abdulhadi, K. F. Uktamov, F. H. Alsultany, S. E. Izzat, M. J. Ansari, H. H. Kzar, M. E. Al-Gazally and E. Kianfar, Nanofluids: properties and applications, *J. Sol-Gel Sci. Technol.*, 2022, 1–35.
7 M. Yasir, M. Khan, M. Sarfraz, D. Abuzaid and M. Z. Ullah, Exploration of the dynamics of ethylene glycol conveying copper and titania nanoparticles on a stretchable/shrinkable curved object: Stability analysis, *Int. Commun. Heat Mass Transfer*, 2022, **137**, 106225.
8 M. Sarfraz and M. Khan, Significance of ethylene glycol-based CNT Homann nanofluid flow over a biaxially stretching surface, *Waves Random Complex Media*, 2022, 1–15.
9 M. Sarfraz and M. Khan, Thermodynamic irreversibility analysis of water conveying argentum and titania nanoparticles subject to inclined stretching surface, *Phys. Scr.*, 2023, **98**(2), 025205.
10 Y. Yang, S. Zheng and Q. Lu, Numerical solutions of non-gray gases and particles radiative transfer in three-dimensional combustion system using DRESOR and SNBCK, *Int. J. Therm. Sci.*, 2021, **161**, 106783.
11 M. Yasir, M. Khan, A. S. Alqahtani and M. Y. Malik, Heat generation/absorption effects in thermally radiative mixed convective flow of Zn–TiO2/H2O hybrid nanofluid, *Case Stud. Therm. Eng.*, 2023, **45**, 103000.
12 G. M. Moldoveanu, G. Huminic, A. A. Minea and A. Huminic, Experimental study on thermal conductivity of stabilized Al2O3 and SiO2 nanofluids and their hybrid, *Int. J. Heat Mass Transfer*, 2018, **127**, 450–457.
13 L. Zheng, J. Niu, X. Zhang and L. Ma, Dual solutions for flow and radiative heat transfer of a micropolar fluid over stretching/shrinking sheet, *Int. J. Heat Mass Transfer*, 2012, **55**(25–26), 7577–7586.
14 T. R. Mahapatra, S. K. Nandy and I. Pop, Dual solutions in magnetohydrodynamic stagnation-point flow and heat transfer over a shrinking surface with partial slip, *J. Heat Transfer*, 2014, **136**(10), 104501.
15 M. N. Rostami, S. Dinarvand and I. Pop, Dual solutions for mixed convective stagnation-point flow of an aqueous silica–alumina hybrid nanofluid, *Chin. J. Phys.*, 2018, **56**(5), 2465–2478.
16 S. M. Mousavi, M. N. Rostami, M. Yousefi, S. Dinarvand, I. Pop and M. A. Sheremet, Dual solutions for Casson hybrid nanofluid flow due to a stretching/shrinking sheet: a new combination of theoretical and experimental models, *Chin. J. Phys.*, 2021, **71**, 574–588.
17 M. I. Asjad, N. Sarwar, M. B. Hafeez, W. Sumelka and T. Muhammad, Advancement of non-newtonian fluid with hybrid nanoparticles in a convective channel and prabhakar's fractional derivative—analytical solution, *Fractal Fract.*, 2021, **5**(3), 99.
18 M. V. Krishna, N. A. Ahamad and A. J. Chamkha, Hall and ion slip effects on unsteady MHD free convective rotating flow through a saturated porous medium over an exponential accelerated plate, *Alexandria Eng. J.*, 2020, **59**(2), 565–577.
19 K. Muhammad, T. Hayat and A. Alsaedi, Heat transfer analysis in slip flow of hybrid nanomaterial (ethylene glycol + Ag+ CuO) *via* thermal radiation and Newtonian heating, *Waves Random Complex Media*, 2021, 1–21.
20 M. V. Krishna and A. J. Chamkha, Hall and ion slip effects on magnetohydrodynamic convective rotating flow of Jeffreys fluid over an impulsively moving vertical plate embedded in a saturated porous medium with ramped wall temperature, *Numer. Methods Partial Differ. Equ.*, 2021, **37**(3), 2150–2177.
21 M. Yasir, M. Sarfraz, M. Khan, A. K. Alzahrani and M. Z. Ullah, Estimation of dual branch solutions for Homann flow of hybrid nanofluid towards biaxial shrinking surface, *J. Pet. Sci. Eng.*, 2022, **218**, 110990.
22 M. V. Krishna and A. J. Chamkha, Hall and ion slip effects on MHD rotating boundary layer flow of nanofluid past an infinite vertical plate embedded in a porous medium, *Results Phys.*, 2019, **15**, 102652.
23 M. V. Krishna, B. V. Swarnalathamma and A. J. Chamkha, Investigations of Soret, Joule and Hall effects on MHD rotating mixed convective flow past an infinite vertical porous plate, *J. Ocean Eng. Sci.*, 2019, **4**(3), 263–275.
24 M. V. Krishna, N. A. Ahamad and A. J. Chamkha, Hall and ion slip effects on unsteady MHD free convective rotating flow through a saturated porous medium over an exponential accelerated plate, *Alexandria Eng. J.*, 2020, **59**(2), 565–577.
25 H. Alkasasbeh, Numerical solution of heat transfer flow of Casson hybrid nanofluid over vertical stretching sheet with magnetic field effect, *CFD Lett.*, 2022, **14**(3), 39–52.
26 Y. Sun and S. Zheng, Influence of particle rotation and partial irradiation on the particle heating up process, *Int. Commun. Heat Mass Transfer*, 2020, **119**, 104892.
27 H. Alkasasbeh, F. M. Al Faqih and A. S. Shoul, Computational Simulation of Magneto Convection Flow of Williamson Hybrid Nanofluid with Thermal Radiation Effect, *CFD Lett.*, 2023, **15**(4), 92–105.
28 M. Yasir, M. Khan, A. S. Alqahtani and M. Y. Malik, Numerical study of axisymmetric hybrid nanofluid MgO-Ag/H2O flow with non-uniform heat source/sink, *Alexandria Eng. J.*, 2023, **75**, 439–446.

29 C. Y. Wang, Liquid film on an unsteady stretching sheet, *Q. Appl. Math.*, 1990, **48**, 601–610.
30 M. Khan and U. Khan, Stability analysis in the transient flow of Carreau fluid with non-linear radiative heat transfer and nanomaterials: critical points, *J. Mol. Liq.*, 2018, **272**, 787–800.
31 N. F. Dzulkifli, N. Bachok, N. A. Yacob, N. Md Arifin and H. Rosali, Unsteady stagnation-point flow and heat transfer over a permeable exponential stretching/shrinking sheet in nanofluid with slip velocity effect: a stability analysis, *Appl. Sci.*, 2018, **8**(11), 2172.
32 N. A. A. Bakar, N. Bachok, N. M. Arifin and I. Pop, Stability analysis on the flow and heat transfer of nanofluid past a stretching/shrinking cylinder with suction effect, *Results Phys.*, 2018, **9**, 1335–1344.
33 R. I. Yahaya, N. Md Arifin and S. S. P. Mohamed Isa, Stability analysis on magnetohydrodynamic flow of Casson fluid over a shrinking sheet with homogeneous-heterogeneous reactions, *Entropy*, 2018, **20**(9), 652.
34 N. S. Ismail, N. M. Arifin, R. Nazar and N. Bachok, Stability analysis of unsteady MHD stagnation point flow and heat transfer over a shrinking sheet in the presence of viscous dissipation, *Chin. J. Phys.*, 2019, **57**, 116–126.
35 I. Waini, A. Ishak and I. Pop, Unsteady flow and heat transfer past a stretching/shrinking sheet in a hybrid nanofluid, *Int. J. Heat Mass Transfer*, 2019, **136**, 288–297.